Durable Nickel-Iron (Oxy)hydroxide Oxygen Evolution Electrocatalysts through Surface Functionalization with Tetraphenylporphyrin

Sinwoo Kang, Changbin Im, Ioannis Spanos, Kahyun Ham, Ahyoun Lim, Timo Jacob, Robert Schlögl, and Jaeyoung Lee*

Abstract: NiFe-based oxides are one of the best-known active oxygen evolution electrocatalysts. Unfortunately, they rapidly lost performance in Fe-purified KOH during the reaction. Herein, tetraphenylporphyrin (TPP) was loaded on a catalyst/electrolyte interface to alleviate the destabilization of NiFe (oxy)hydroxide. We propose that the degradation occurs primarily due to the release of thermodynamically unstable Fe. TPP acts as a protective layer and suppresses the dissolution of hydrated metal at the catalyst/electrolyte interface. In the electric double layer, the nonpolar TPP layer on the NiFe surface also invigorates the redeposition of the active site, Fe, which leads to prolonging the lifetime of NiFe. The TPP-coated NiFe was demonstrated in anion exchange membrane water electrolysis, where hydrogen was generated at a rate of $126\,L\,h^{-1}$ for $115\,h$ at a $1.41\,mV\,h^{-1}$ degradation rate. Consequently, TPP is a promising protective layer that could stabilize oxygen evolution electrocatalysts.

Introduction

According to the International Renewable Energy Agency, a 76% energy efficiency for 20 years is essential[1] to achieve the goal of hydrogen production level at a cost close to or less than $2 kg^{-1}$ set by the U.S. Department of Energy.[2] In fact, anion exchange membrane water electrolysis (AEMWE) has been considered a promising pathway for large-scale green hydrogen production at low costs owing to the use of non-precious catalyst materials. One of the main components of anion exchange water electrolyzers is the membrane electrode assembly (MEA), which is mainly composed of a porous transport layer, an anion exchange membrane (AEM), and a catalyst layer. Under alkaline conditions, hydroxyl anions produced by water reduction at the cathode act as charge carriers. The oxygen evolution reaction (OER) follows a four-step pathway using hydroxyl ions and is the most sluggish process in the entire AEMWE system. The catalyst layer in the anode plays an essential role in the AEMWE performance as it significantly diminishes the overpotential.[3]

NiFe-based (oxy)hydroxides are state-of-the-art performance and non-noble oxygen evolution electrocatalysts.[4] The reaction mechanism of NiFe-based catalysts, however, still has been controversial over the past decades. Previous studies have regarded Ni as the active site;[5–10] however, in recent studies, Fe[9,11–21] or Ni–Fe dual active sites[22–24] have also been considered. Despite the complexity of heterogeneous catalysis, in situ/operando measurements and density functional theory (DFT) calculations have determined Fe as the ultimate active site.[15,16,18] On the other hand, the ambiguity of mechanistic understanding also limits an improvement in the stability of the NiFe-based (oxy)hydroxides for applications and the commercialization of AEMWE. Numerous studies so far have reported that

[*] S. Kang, Dr. K. Ham, Prof. Dr. J. Lee
School of Earth Sciences and Environmental Engineering,
Gwangju Institute of Science and Technology (GIST)
Gwangju 61005 (Republic of Korea)
E-mail: jaeyoung@gist.ac.kr

S. Kang, Dr. K. Ham, Prof. Dr. J. Lee
International Future Research Center of Chemical Energy Storage
and Conversion Processes (ifRC-CHESS), GIST
Gwangju 61005 (Republic of Korea)

C. Im, Prof. Dr. T. Jacob
Institute of Electrochemistry,
Ulm University
Ulm (Germany)

Dr. I. Spanos, Dr. A. Lim, Prof. Dr. R. Schlögl
Department of Heterogeneous Reactions,
Max Planck Institute for Chemical Energy Conversion
Stiftstrasse 34–36, 45470, Mülheim an der Ruhr (Germany)

Dr. K. Ham, Prof. Dr. J. Lee
Ertl Center for Electrochemistry and Catalysis, GIST
Gwangju 61005 (Republic of Korea)

Prof. Dr. T. Jacob
Helmholtz-Institute Ulm (HIU) Electrochemical Energy Storage,
Ulm (Germany)

Prof. Dr. T. Jacob
Karlsruhe Institute of Technology (KIT),
Karlsruhe (Germany)

Prof. Dr. R. Schlögl
Department of Inorganic Chemistry,
Fritz Haber Institut der Max-Planck-Gesselschaft
Faradayweg 4–6, 14195 Berlin (Germany)

NiFe-based materials have low durability in Fe-purified KOH , and the strategy to prolong the lifetime of these catalysts is still in its early stages.[25–28,28,29] Chung et al.[18] reported that the lack of Fe adsorption by the substrate restricts the redeposition of Fe. Furthermore, Kuai et al.[30] reported that the catalyst performance diminishes because site-selective Fe redeposition agglomerate Fe as FeOOH (particle), which is in accordance with the results of other studies.[12,17] Farhat et al.[31] reported that although surface Fe promotes high OER catalysis in ultra-thin and thicker NiFe-oxo/hydroxide films, an exchange causing surface Fe to move into higher coordination bulk Fe results in the loss of OER activity in the activated NiFe-oxo/hydroxide in the Fe-free electrolyte. Recent studies have focused on OER catalyst modification to reduce degradation. Peng et al.[26] suggested the importance of vacant sites in metals, which strengthen the Fe–O bond and alleviate lattice distortion, thus suppressing Fe dissolution. Feng et al.[32] introduced Co into NiFe as an in situ Fe redeposition promoter. Chung et al.[18] succeeded in increasing the Fe adsorption energy by incorporating Cu into the Ni matrix and enhancing the number of Fe on the electrode. The new viewpoint that the Fe simultaneously repeats the dissolution-redeposition enabled the strategy to control the dissolution from the catalyst/electrolyte interface. Beck et al.[33] and Klaus et al.[34] reported that Fe is eluted as FeO_4^{2-} in alkaline electrolyte and hydrated since it leaves the electrode. We hypothesized that the nonpolar interface layer on NiFe-based material could enhance the concentration of redeposition reactant.

Herein, a strategy to reinforce a labile NiFe catalyst by manipulating the polarity of the electric double layer was developed. The dissolution behavior of Fe from its host material, $Ni(OH)_2$, was also investigated. Online electrochemical flow cell inductively coupled plasma-optical emission spectroscopy (online EFC ICP-OES)[35–37] allowed the real-time quantification of the metal dissolution rate during the OER. The loss of Fe was severe in the bare NiFe-based catalyst, while nonpolar tetraphenylporphyrin (TPP) minimized the dissolution of Fe by phase engineering near the electric double layer. Inhibition of Fe dissolution increased the lifetime in the double layer and eventually increasing the Fe redeposition. The role of TPP was validated in AEMWE at $500\,mA\,cm^{-2}$ under conditions well aligned with practical commercial-scale electrolysis, effectively suppressing the degradation rate.

Results and Discussion

It is hypothesized that the TPP layer could filter out the hydrated ions from the bilayer while increasing the concentration of the redeposition reactant. To prove the hypothesis, we simulated the energy barrier required for FeO_4^{2-} species to permeate the TPP through nudged elastic band (NEB) calculations (Figure 1a). It was confirmed that the energy barrier of $\approx 10\,eV$ indicates that the TPP penetration is hardly applicable. This high energy barrier indirectly suggests that TPP can play as physical barrier from Fe dissolution by preventing the protonation of the Fe–O
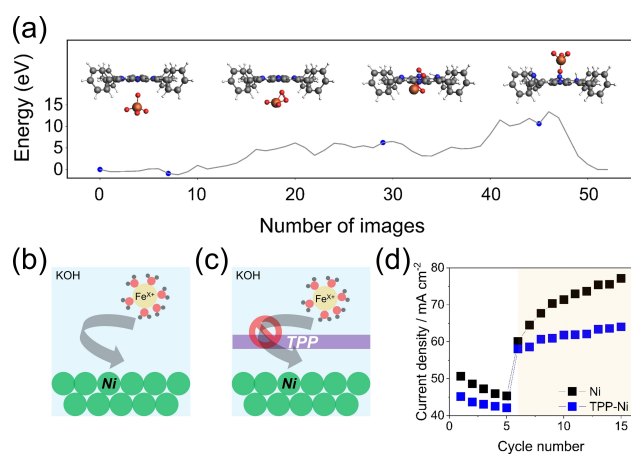
Figure 1. a) NEB method was applied for the calculation of the energy barriers for $[FeO_4]^{2-}$ to pass through TPP. (blue: N atoms, dark gray: C atoms, white: H atoms, red: O atoms, orange: Fe atoms) Schematic illustration of the model experiment to verify the role of TPP for filtering hydrated Fe in b) Ni and c) TPP-Ni. d) 15 CV measurements in Fe-purified KOH (1.0 M) (white area) and KOH (1.0 M) containing Fe (50 µg L⁻¹) (orange area) to observe the activation attenuation effect by TPP filtering the entrance of Fe into the electrode.

site.[38] This indicates that the TPP nonpolar layer might effectively block the hydrated Fe ions from the electrode and bulk electrolyte. The TPP layer might filter the hydrated Fe ion exiting from the double layer concurrently increasing the concentration of the redeposition reactant. To further investigate the role of the TPP layer, an additional model experiment was performed on a bare Ni electrode (Figure 1b) and TPP-loaded Ni (TPP-Ni) (Figure 1c). First, five cyclic voltammetry (CV) cycles were performed in Fe-purified KOH (1.0 M) (Figure 1d). The initial activity was higher in Ni ($50.7\,mA\,cm^{-2}$) than in TPP-Ni ($45.1\,mA\,cm^{-2}$) at 1.935 potential relative to reversible hydrogen electrode (V_{RHE}) OER potential, which indicated that the TPP coating on Ni might have blocked some active sites. The degradation speed was lower in TPP-Ni ($-0.6\,mA\,cm^{-2}\,cycle^{-1}$) than in Ni ($-1.1\,mA\,cm^{-2}\,cycle^{-1}$). Upon changing the electrolyte to KOH (1.0 M) containing Fe ($50\,\mu g\,L^{-1}$) in the 6th CV cycle, the activity of TPP-Ni increased by approximately 135 %. This can be attributed to the well-known synergistic effect of Fe when intercalated to a NiO_xH_y substrate.[6,39] In particular, the increase in the activity rate of TPP-Ni ($0.59\,mA\,cm^{-2}\,cycle^{-1}$) was suppressed compared to that of Ni ($1.71\,mA\,cm^{-2}\,cycle^{-1}$) because the activation was derived from the Fe spiking on the Ni electrode from the electrolyte. TPP might have filtered the hydrated Fe ion adsorption on the Ni matrix. Fe is the active site in NiFe-based alkaline OER electrocatalysts, and its loss results in a major degradation mechanism.[18] Consequently, applying TPP as a protecting layer on the NiFe OER electrode is essential to increase the stability of the anode. As shown in Figure 2a, TPP-Fe-spiked NiO_xH_y (TPP-FSN) catalyst is prepared by a facile 3-step procedure from the $Ni(OH)_2$ electrodeposited substrate layer on a carbon paper (CP). Fe was spiked on the $Ni(OH)_2$ substrate to maximize the high turnover
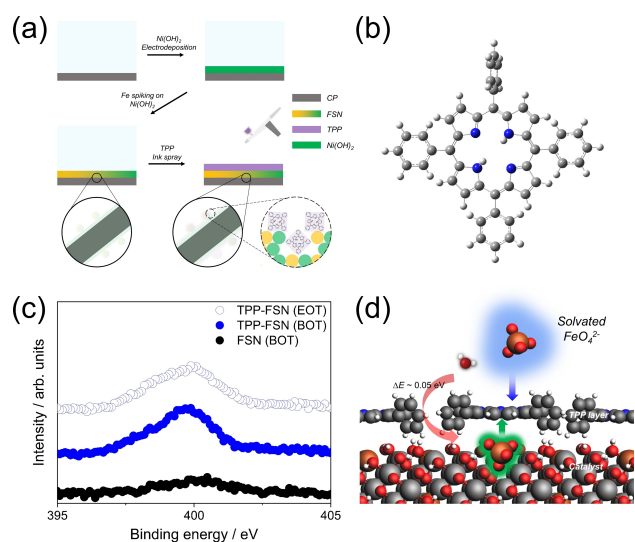
Figure 2. a) Three-step procedure for TPP-FSN catalyst preparation. The first step involved the cathodic electrodeposition of Ni(OH)$_2$ on CP substrate. The second step was the preparation of FSN by cycling 50 times in a Fe precursor (1 mM) containing the KOH electrolyte (1.0 M). The final step was TPP loading on the electrodeposited FSN electrode by spray-coating. b) Molecular structure of TPP (blue: N atoms, gray: C atoms, white: H atoms). c) High-resolution XPS N 1s profiles of FSN (BOT), TPP-FSN (BOT), and TPP-FSN (EOT). d) The side-view of the optimized geometry of the TPP on FSN. (blue: N atoms, dark gray: C atoms, white: H atoms, red: O atoms, orange: Fe atoms, light gray: Ni atoms)

frequency of Fe by exposing it to the surface, forming Fe-spiked NiO$_x$H$_y$ (FSN).[39] Electrodeposited Ni(OH)$_2$ showed a spherical morphology on the carbon fibers (Figures S1a and b). Fe spiking on the Ni(OH)$_2$ substrate resulted in FeOOH phase (526 and 690 cm^{-1}), where Fe was inserted into the Ni lattice (Figure S2), which was in agreement with the result of a previous study.[40] Scanning electron microscopy with energy dispersive spectroscopy (SEM-EDS) indicated that the resulting FSN had an Fe:Ni ratio of 2:8, which was verified as the optimum Fe content (10–25 %) by several studies (Table S1b).[6,9,12,17,39,41] Surface-sensitive X-ray photoelectron spectroscopy (XPS) revealed an Fe:Ni ratio of 4:6, which indicated that most Fe was placed on the surface owing to the Fe spiking of the Ni matrix (Table S1a). The TPP ink (0.1 mM TPP in acetonitrile/tetrahydrofuran) was sprayed onto the FSN over CP (TPP-FSN). TPP consists of four pyrrole rings with nitrogen atoms oriented inside the ring and is surrounded by four benzene rings as pendent groups (Figure 2b). TPP has a symmetric structure, hydrophobic property, and nonpolar nature. The stability of TPP (protective layer) onto the metal oxide catalyst, TPP-FSN was verified by three approaches. First, the double-layer capacitance (C$_{dl}$) changed (Figure S3). The FSN electrodeposition on the CP increased from 18 to 49 μF cm^{-2}, while the TPP loading on the FSN increased from 49 to 257 μF cm^{-2}. This change verified the successful loading of the porous layer of TPP on FSN, which is in agreement with the results reported by Li et al., who detected Fe-TPP[Cl] on the Cu electrode by monitoring the C$_{dl}$ change.[42]

SEM visualized the change in morphology after TPP loading, demonstrating the porous layer spread homogeneously on the FSN (Figures S1c and d). Second, a square planar nitrogen ring was detected by XPS N 1s (Figure 2c). The binding energy of 400 eV emerged when TPP was loaded onto the FSN at the beginning-of-test (BOT), which is in accordance with the results of Daniel et al.[43] Compared to FSN, N was successfully quantified in TPP-FSN. When TPP was loaded onto the FSN, the nitrogen content changed from 1 % to 3 % (1 % owing to the nitrate precursor residue during FSN fabrication) (Table S1c). Moreover, its unique structure remained even at the end-of-test (EOT, 1500 CV scans of OER in the range of 0.935–1.935 V$_{RHE}$). Finally, NiOOH (480 and 560 cm^{-1}) and FeOOH (526 and 690 cm^{-1}) species in the as-synthesized FSN were detected by Raman spectroscopy (Figure S2).[40] The intense signature peak of TPP swamped all signals of the FSN, thus indicating the successful coverage of TPP on FSN.[44] Adsorption energy and the stability of TPP on FSN surface were estimated using ReaxFF molecular simulation[45,46] to handle the large system size. The optimized geometry of the TPP on FSN was verified as both on-top Fe and Ni sites and adsorption energy depicted. (Figures 2d, S4a, and b). It is difficult to cover the adsorption degree of freedom on the disordered surface including the defects, coverages, and microstructures. Therefore, only the fixed number of Fe spike models and a single adsorption layer of TPP were considered. From the optimized geometry, the hydrogen bonding between OH$_{ads}$ on M (M = Ni or Fe) and the N atom from the pyrrole ring (N–H···HO–M) mainly stabilized the TPP-FSN interface (Figure S4c). Additionally, the π···HO interaction and the hydrogen bonding between the phenyl H···OH–M softly strengthened the adsorption of TPP on FSN, which is in accordance with the results of a previous study (Figure S4d).[47] Although TPP adsorption on the Fe site was stronger than on the Ni site by 0.21 eV, both sites should be considered adsorption sites because they are both energetically favored (averaged of −2.45 eV for the Fe site and −1.90 eV for the Ni site, respectively) and surface coverage of the exposed Ni or Fe species rules more markedly than individual energetics (Table S2).

Online EFC ICP-OES was conducted to visualize the real-time degradation of the (TPP-)FSN OER catalysis using a home-made cell (Figure 3a). Stress tests of the OER current at chronopotentiometry values of 10 and 20 mA cm^{-2} for 30 min were mixed with an open circuit potential for 20 min before and after the OER operation (Figure 3b). The concentrations of Fe (Figure 3c) and Ni (Figure S5) were quantified along with the OER current density. When considering the dissolution rate per unit area, the Ni dissolution rate of Ni (7.9 pg s^{-1} cm^{-2}) was 11 times less when Fe was incorporated into the Ni matrix as FSN (0.7 pg s^{-1} cm^{-2}) at 10 mA cm^{-2} (Figure 3d). This is consistent with a previous study by Spanos et al.,[36] where Fe acted as an active site and a stabilizer of the Ni matrix. However, FSN demonstrated rapid Fe dissolution (20.9 pg s^{-1} cm^{-2}) during the OER operation, which is in accordance with the results of a previous study where Ni showed a lower dissolution rate (0.7 pg s^{-1} cm^{-2}), based on DFT[26] calcula-
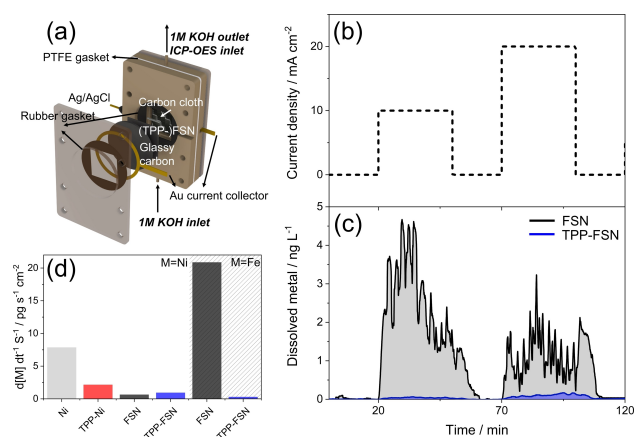
Figure 3. a) Online EFC ICP-OES cell. b) Chronopotentiometry protocol during online EFC ICP-OES. c) Transient analysis of the eluted Fe from the FSN and TPP-FSN catalyst in Fe-purified KOH (1.0 M) during the stress test. d) Metal dissolution rate per unit area achieved from chronopotentiometric measurement at 10 mA cm^{-2} for 30 min.

Figure 4. a) CV experiment for activity and stability tests in a half-cell. b) Overpotential comparison against cycle number. Error bars represent the standard deviation of triplicate measurements. c) Schematic representation of 9 cm^2 MEA with cell hardware. d) Voltage profile along 115 h of TPP-FSN in 500 mA cm^{-2}. Gas products of AEMWE (H$_2$-filled, O$_2$-void rectangular) were quantified along with the long-term stability test. All membranes are 50-μm-thick X37-50 grade T. Cell temperature was set as 60 °C. KOH (1.0 M) was fed at a flow rate of 36 mL min^{-1}.

tions and in situ ICP mass spectroscopy (ICP-MS)[18] results at 10 mA cm^{-2}. This result excluded NiFe destabilization from the surface-Fe diffusion to the inside of the lattice (bulk Fe).[31] A higher dissolution rate was observed at 10 mA cm^{-2} than at 20 mA cm^{-2}, which is attributed to the surface reconstruction process in the initial step of the OER, which accelerated the Fe dissolution (Figure 3c).[48,49] Knöppel et al.[50] reported that an oxygen evolution electrocatalyst stabilizes over time after severe dissolution in the beginning (<1 h). TPP also filtered the Ni dissolution (Ni: 7.9 and TPP-Ni: 2.2 pg s^{-1} cm^{-2}), as observed in the first 5 CV cycles (Figure 1d). In particular, TPP-FSN significantly suppressed Fe dissolution to 0.3 pg s^{-1} cm^{-2} as compared to that of FSN (20.9 pg s^{-1} cm^{-2}) at 10 mA cm^{-2}. This was also observed at the 20 mA cm^{-2} OER operation. Geiger et al.[51] performed lifetime calculations where FSN revealed a lifetime of 3.2 d as compared to 219.8 d for TPP-FSN, thus showing that TPP-FSN had a 69-fold lifetime increase. The TPP layer on the FSN kept the Fe population on the surface of the OER catalyst. This observation is in accordance with the quantification results of the metal content from XPS and SEM-EDS (Tables S1a and b).

All electrochemical measurements were performed in a polymer-based electrochemical cell (polytetrafluoroethylene and polyetheretherketone) to prevent glass etching.[52] Fe was thoroughly purified from KOH (1.0 M),[6] and the Fe purification results were verified by ICP-MS (Figure S6) and electrochemical tests (Figure S7) in bare carbon. A graphite rod counter electrode was used to address Pt dissolution.[53–55] The reference electrode was calibrated using an RHE with the value of the hydrogen oxidation/evolution reaction from the x-intercept (Figure S8).[56] The activity and durability of FSN and TPP-FSN were compared using CV tests (Figure 4a). The substrate CP and additive TPP did not exhibit considerable anodic currents in the 1.2–1.7 V$_{RHE}$ range, thus confirming their inactivity toward OER. In the first CV, FSN and TPP-FSN exhibited similar activity (352 mV@30 mA cm^{-2}), indicating that TPP loading

did not affect the initial activity in triplicate measurements (Figure 4b). To estimate the energy barrier due to the presence of TPP, NEB calculations were performed along the various pathways. The relative energy barrier calculation for OH to travel around TPP-FSN was approximately 0.1–0.4 eV near the phenyl ring and less than 0.05 eV at the other sides (Figures 2d, S9, and S10), which indicated that mostly, the reactant could diffuse following the latter pathways to the active site with the trivial energy barrier. The locally captured reactants, rather than the repulsive reactants from the hydrophobicity, leads to the local rearrangement of the phenyl ring, which however seems not to influence the overall OER potential. Remarkably, TPP-FSN showed much less activity loss after EOT. The FSN overpotential increased from 352 to 374 mV, showing an increase of 22 mV after EOT at 30 mA cm^{-2}, while the TPP-FSN overpotential increased from 352 to 362 mV, demonstrating an increase of 10 mV under the same stability test conditions (Figure 4b). Similar trends were observed at 50 mA cm^{-2} ($\Delta\eta_{FSN}=24$ mV and $\Delta\eta_{TPP-FSN}=12$ mV), and the experiments were performed in triplicates. To determine the effect of TPP loading on the mechanism, Tafel slopes were compared. No mechanism change was observed in the catalysis with FSN (51 mV dec^{-1}) and TPP-FSN (58 mV dec^{-1}) (Figure S11). Corresponding microkinetic studies indicated that M–O$_{ads}$/M–OOH$_{ads}$ was the rate-determining step (RDS).[57] Bai et al.[40] also concluded by operando Raman spectroscopy that FeOOH–NiOOH OER electrocatalysis suffers from the second electron transfer reaction as the RDS. The Tafel slope of FSN increased to 64 mV dec^{-1} (ΔFSN = 13 mV dec^{-1}) at EOT, indicating poor OER kinetics in the same RDS. However, the TPP-FSN Tafel slope increment decreased by six times (ΔTPP-FSN = 2 mV dec^{-1}), thus

indicating that the TPP buffered OER kinetic worsening after EOT. The changes in charge transfer resistance (ΔR_{CT}) for FSN and TPP-FSN, examined by electrochemical impedance spectroscopy (EIS), were 0.96 and 0.29 Ω, respectively (Figure S12). A series of electrochemical tests (CV, Tafel analysis, and EIS) reproduced the stability enhancement role of TPP in FSN OER catalysis, when the TPP loading amount was evaluated at 1, 2, and 3 mL cm^{-2} (Figure S13). A less stable OER performance was demonstrated at 1 and 3 mL cm^{-2}, due to the lack of loading and overloading, respectively. This observation showed that insufficient TPP loading (1 mL cm^{-2}) was inefficient as compared to the optimal loading amount (2 mL cm^{-2}). Furthermore, overloading might lead to the agglomeration of TPP (3 mL cm^{-2}), and a similar result was shown in the ionomer content optimization in MEA.[58] Consequently, the optimal amount of TPP loaded (2 mL cm^{-2}) on FSN was employed in all experiments. The Ni(OH)$_2$/NiOOH peak intensity reflects the electrochemical surface area (ECSA) of the Ni atom directly contacting the electrolyte. The TPP-FSN shrinkage of 1.42 mA cm^{-2} as compared to 1.75 mA cm^{-2} for FSN at the first cycle (Figure S14) supported the hypothesis that TPP partially blocks the Ni site when forming hydrogen bonds with FSN. Notably, the redox intensity of TPP-FSN steadily increased through 1500 CV cycles and reached 2.05 mA cm^{-2}. In contrast, the redox intensity of FSN decreased to 1.5 mA cm^{-2}. This is due to the detachment of the weakly adsorbed TPP at 1–500 CV cycles in TPP-FSN, and the trace amount of dissolved Fe redeposition on the clean NiO$_x$H$_y$ surface. Fe concentration in 1 M KOH electrolyte after 500 CV was measured by ICP-MS (Figure S6). The difference in Fe amount increment after 500 CV in the electrolyte (ΔFe_{FSN}: 12 µg L^{-1}, $\Delta Fe_{TPP-FSN}$: 3.8 µg L^{-1}) made the different behavior of Ni redox peak. Boettcher et al. reported that NiOOH OER cycling in Fe-containing electrolytes exhibited a decrease in the Ni redox peak,[6,39] which indicates that Fe impurities covered the Ni site, thus lowering Ni ECSA. This observation further proved the role of TPP in preventing the liberation of eluted Fe into the electrolyte during OER catalysis. The application of TPP in AEMWE was then evaluated (Figure 4c). The MEA was prepared by the catalyst-coated-membrane method using a commercial Pt/C (cathode) on a commercial AEM. The experiments were performed at 60 °C in KOH (1.0 M) and MEA (9 cm^2), with real-time detection of the product gases (H$_2$/O$_2$). Chronopotentiometry measurement was conducted at 500 mA cm^{-2} for 115 h at a 1.41 mV h^{-1} degradation rate, which was lower than the degradation rate during the first 25 h (1.56 mV h^{-1}) (Figure 4d). This result was in accordance with those obtained by Knöppel et al.,[50] where the S-number,[51] a metric for electrocatalyst stability, drastically increased over time in a single cell. This value is in agreement with recently published papers under similar operating conditions (cathode catalyst: platinum group metal (PGM), anode catalyst: non-PGM, 1.0 M KOH , and 45–70 °C cell temperature) ranging from 1 to 2 mV h^{-1}.[59–62] Furthermore, a 126 L h^{-1} H$_2$ flow rate and 62 L h^{-1} O$_2$ flow rate showed a 91 % faradaic efficiency, that is beneficial for the practical application of

non-PGM anode electrocatalyst-based AEMWE. These results provide insights into the material design strategy for minimizing metal dissolution in metal-based catalysts.

To investigate the stability enhancement after TPP loading, three deactivation mechanisms, dissolution,[18] agglomeration,[30] and bulkization,[31] were considered (Figure S15). The Fe portion (Fe/(Fe+Ni)) at the surface and bulk decreased by approximately 35 % in FSN, while with TPP-FSN, it only dropped approximately 12 % after EOT (Table S1). This implied that the Fe in the bulk and at the surface was eluted in OER catalysis and that TPP blocked the dissolution from the electrode. Metal agglomeration was excluded based on X-ray absorption spectroscopy (XAS) at the Fe K-edge (Figure 5a). Both FSN and TPP-FSN at BOT had a singlet pre-edge peak at 7114 eV, resembling that of FeOOH,[30] which is in agreement with the results of Raman spectroscopic analysis. The peak was split into a doublet at EOT, indicating that FeO and Fe$_2$O$_3$ were redeposited after the elution of FeOOH in the electrolyte. A doublet peak verified the presence of Fe^{3+} T$_d$ coordination from the Fe$_2$O$_3$ phase as compared to FeOOH (Fe^{3+} O$_h$), which is expressed as a singlet peak.[63] Agglomerated FeOOH, which deteriorates the stability,[30] was not observed at EOT. In contrast, the dissolution/redeposition dynamics formed a new phase (FeO/Fe$_2$O$_3$) in TPP-FSN. It is plausible that surface atom liberation from the electrode (dissolution) is the primary cause of the TPP-FSN degradation after ruling out the agglomeration and bulkization of Fe.
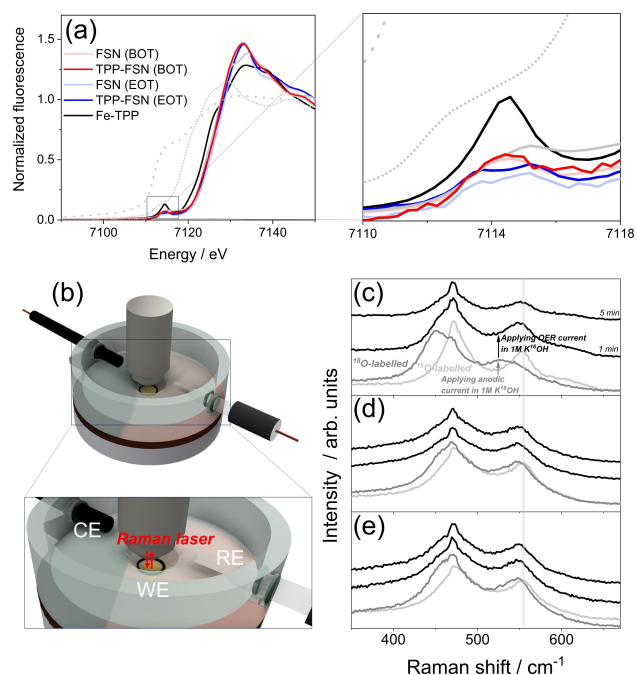
Figure 5. a) XAS spectra of the (TPP-)FSN at BOT and EOT in the Fe K-edge. (gray dotted line: Fe film, short dotted line: FeO, solid line: Fe$_2$O$_3$ reference) b) in situ Raman cell. In situ Raman spectra of c) Ni, d) FSN, and e) TPP-FSN. ^{18}O-labeling was conducted in K^{18}OH (1 M) applying 21 mA cm^{-2} anodic current for 30 min. ^{18}O-labeled samples then moved to fresh K^{16}OH (1 M) and 1.2 mA cm^{-2} of OER current was applied.

The stability enhancement origin after TPP loading on FSN has three candidates: **(1)** the remnant of Fe in the electrode without agglomeration, **(2)** the anchored Fe by the four nitrogen-containing pyrrole rings (N4) in TPP, and **(3)** OER mechanism shift from lattice oxygen participation mechanism (LOM) to adsorbate evolution mechanism (AEM). To rule out scenario **(2)**, XAS was employed to detect the location of Fe on the electrode (Figure 5a). An interaction between the eluted Fe and N4 in TPP was not observed due to the absence of the Fe–N4 of Fe-TPP reference intense pre-edge signature peak at 7114.6 eV (black line). However, doublet peaks at 7113.7 and 7115.2 eV were attributed to FSN and TPP-FSN at EOT, respectively. Consequently, Fe remained in the electrode layer during the stability test in OER. Furthermore, the Ni–N4 structure was not observed, which indicated that the hydrated Ni cannot be coordinated by N4 in TPP (Figure S16). The amount of metal dissolution is affected by the OER mechanism.[51] LOM which forms the O vacancies disrupts the stability of the catalyst. To rule out **(3)**, ^{18}O-labeling experiments coupled with in situ Raman spectroscopy were employed to probe the OER mechanism of FSN and TPP-FSN. Experiments were conducted using home-made in situ electrochemical Raman cell in 1 M Fe-purified KOH electrolyte **(Figure 5b)**. ^{16}O–Ni showed the $\delta(Ni^{3+}-O)$ (472 cm^{-1}) and $\nu(Ni^{3+}-O)$ (555 cm^{-1}) in 1.2 mA cm^{-2} OER current density **(Figure 5c)**. ^{18}O isotope labeling was conducted by applying 21 mA cm^{-2} of anodic current for 30 min in 1 M K^{18}OH. This process red-shifted $\delta(Ni^{3+}-O)$ (449 cm^{-1}) and $\nu(Ni^{3+}-O)$ (530 cm^{-1}) by about 25 cm^{-1}, which is in agreement with previous studies[64,65] indicating $^{18}OH^-$ from electrolyte was incorporated into lattice oxygen. As-synthesized ^{18}O–Ni was applied in OER current (1.2 mA cm^{-2}) with 1 M K^{16}OH, the peaks were blue-shifted back to the original position indicating lattice ^{18}O was directly substituted by electrolyte ^{16}O. This is the fingerprint of the LOM occurring on pure Ni catalyst in alkaline OER inducing harsh metal dissolution.[64] However, in the case of FSN **(Figure 5d)** and TPP-FSN **(Figure 5e)**, no dramatic ^{18}O labeling was observed since their peak was only 7 cm^{-1} red-shifted ($\delta(Ni^{3+}-O)$ (469 cm^{-1}) and $\nu(Ni^{3+}-O)$ (548 cm^{-1})). And their ^{18}O labeled peak was sustained in the ^{18}O labeled form and was not directly placed back to the ^{16}O. This is in agreement with the previous study[64] that Fe-incorporated NiO$_x$H$_y$ samples follow the AEM and TPP-FSN also does not change the OER mechanism. Our result in Figure 3d, that Ni dissolution suppression after incorporation of Fe also supports the fact Fe incorporation induces the mechanism shift from LOM to AEM. Similar Tafel slope (ca. 60 mV dec^{-1}) in Figure S11 indicates that FSN and TPP-FSN both have the same RDS strengthening TPP does not influence the oxygen-evolving pathway of FSN. Those results also rule out the possibility of **(3)** that TPP enhances the stability of FSN by changing the OER pathway from LOM to AEM. Fully hydrated FeO$_4^{2-}$ species redeposition occurs dynamically.[18,33,34] The TPP protective layer then prohibits its complete dissolution to bulk electrolyte. TPP doesn't change the OER mechanism of FSN and elongates the lifetime near the electrode and enlarges the concentration of redeposition reactant by forming a nonpolar layer.

Conclusion

In conclusion, the factors resulting in the destabilization and strategy for reinforcement of NiFe-based catalysts (FSNs) in alkaline OER catalysis were investigated. The detailed electrochemical and spectroscopic analyses revealed that Fe population decrement by its dissolution was the main deactivation pathway. The loading of nonpolar TPP on FSN acted as a barrier for the hydrated Fe to remain in the electric double layer. TPP enhanced the lifetime of the eluted Fe in the electric double layer and facilitated its redeposition on the FSN catalyst. Upon TPP coating, the durability of the catalyst increased without changing oxygen evolving mechanism. Furthermore, the role of TPP in enhancing the stability of AEMWE was confirmed. High-current-density chronopotentiometric operation (500 mA cm^{-2}) with TPP-loaded FSN maintained a long-term OER activity (115 h) with a substantial H$_2$ evolution (rate of $\approx$126 L h^{-1}). This improved mechanistic understanding of FSN provides insights into the future development of durable electrocatalysts for water electrolysis.

Conflict of Interest

The authors declare no conflict of interest.

Data Availability Statement

The data that support the findings of this study are available from the corresponding author upon reasonable request.

[1] U. S. Department of Energy, *FY 2019 Progress Report for the DOE Hydrogen and Fuel Cells Program*, Washington, DC, **2020**.

[2] International Renewable Energy Agency, *Green Hydrogen Cost Reduction: Scaling up Electrolysers to Meet the 1.5°C Climate Goal*, Abu Dhabi, **2020**.

[3] E. Fabbri, T. J. Schmidt, *ACS Catal.* **2018**, 8, 9765–9774.

[4] C. C. L. McCrory, S. Jung, J. C. Peters, T. F. Jaramillo, *J. Am. Chem. Soc.* **2013**, *135*, 16977–16987.

[5] M. W. Louie, A. T. Bell, *J. Am. Chem. Soc.* **2013**, *135*, 12329–12337.

[6] L. Trotochaud, S. L. Young, J. K. Ranney, S. W. Boettcher, *J. Am. Chem. Soc.* **2014**, *136*, 6744–6753.

[7] B. J. Trześniewski, O. Diaz-Morales, D. A. Vermaas, A. Longo, W. Bras, M. T. M. Koper, W. A. Smith, *J. Am. Chem. Soc.* **2015**, *137*, 15112–15121.

[8] O. Diaz-Morales, D. Ferrus-Suspedra, M. T. M. Koper, *Chem. Sci.* **2016**, *7*, 2639–2645.

[9] H. S. Ahn, A. J. Bard, *J. Am. Chem. Soc.* **2016**, *138*, 313–318.

[10] N. Li, D. K. Bediako, R. G. Hadt, D. Hayes, T. J. Kempa, F. von Cube, D. C. Bell, L. X. Chen, D. G. Nocera, *Proc. Natl. Acad. Sci. USA* **2017**, *114*, 1486–1491.

[11] Y.-F. Li, A. Selloni, *ACS Catal.* **2014**, *4*, 1148–1153.

[12] D. Friebel, M. W. Louie, M. Bajdich, K. E. Sanwald, Y. Cai, A. M. Wise, M.-J. Cheng, D. Sokaras, T.-C. Weng, R. Alonso-Mori, R. C. Davis, J. R. Bargar, J. K. Nørskov, A. Nilsson, A. T. Bell, *J. Am. Chem. Soc.* **2015**, *137*, 1305–1313.

[13] J. Y. C. Chen, L. Dang, H. Liang, W. Bi, J. B. Gerken, S. Jin, E. E. Alp, S. S. Stahl, *J. Am. Chem. Soc.* **2015**, *137*, 15090–15093.

[14] Z. K. Goldsmith, A. K. Harshan, J. B. Gerken, M. Vörös, G. Galli, S. S. Stahl, S. Hammes-Schiffer, *Proc. Natl. Acad. Sci. USA* **2017**, *114*, 3050–3055.

[15] B. M. Hunter, N. B. Thompson, A. M. Müller, G. R. Rossman, M. G. Hill, J. R. Winkler, H. B. Gray, *Joule* **2018**, *2*, 747–763.

[16] J. M. P. Martirez, E. A. Carter, *J. Am. Chem. Soc.* **2019**, *141*, 693–705.

[17] S. Lee, L. Bai, X. Hu, *Angew. Chem. Int. Ed.* **2020**, *59*, 8072–8077; *Angew. Chem.* **2020**, *132*, 8149–8154.

[18] D. Y. Chung, P. P. Lopes, P. Farinazzo Bergamo Dias Martins, H. He, T. Kawaguchi, P. Zapol, H. You, D. Tripkovic, D. Strmcnik, Y. Zhu, S. Seifert, S. Lee, V. R. Stamenkovic, N. M. Markovic, *Nat. Energy* **2020**, *5*, 222–230.

[19] L. Bai, C.-S. Hsu, D. T. L. Alexander, H. M. Chen, X. Hu, *Nat. Energy* **2021**, *6*, 1054–1066.

[20] S. Kang, K. Ham, H.-K. Lim, J. Lee, *Electrochim. Acta* **2021**, *386*, 138401.

[21] J. Park, S. Kang, J. Lee, *J. Mater. Chem. A* **2022**, *10*, 15975–15980.

[22] H. Xiao, H. Shin, W. A. Goddard, *Proc. Natl. Acad. Sci. USA* **2018**, *115*, 5872–5877.

[23] H. Shin, H. Xiao, W. A. Goddard, *J. Am. Chem. Soc.* **2018**, *140*, 6745–6748.

[24] C. Wu, X. Zhang, Z. Xia, M. Shu, H. Li, X. Xu, R. Si, A. I. Rykov, J. Wang, S. Yu, S. Wang, G. Sun, *J. Mater. Chem. A* **2019**, *7*, 14001–14010.

[25] S. Li, Z. Li, R. Ma, C. Gao, L. Liu, L. Hu, J. Zhu, T. Sun, Y. Tang, D. Liu, J. Wang, *Angew. Chem. Int. Ed.* **2021**, *60*, 3773–3780; *Angew. Chem.* **2021**, *133*, 3817–3824.

[26] L. Peng, N. Yang, Y. Yang, Q. Wang, X. Xie, D. Sun-Waterhouse, L. Shang, T. Zhang, G. I. N. Waterhouse, *Angew. Chem. Int. Ed.* **2021**, *60*, 24612–24619; *Angew. Chem.* **2021**, *133*, 24817–24824.

[27] Y. Wu, J. Yang, T. Tu, W. Li, P. Zhang, Y. Zhou, J. Li, J. Li, S. Sun, *Angew. Chem. Int. Ed.* **2021**, *60*, 26829–26836; *Angew. Chem.* **2021**, *133*, 27033–27040.

[28] C. Li, L. Xie, J. Zhao, L. Gu, H. Tang, L. Zheng, G. Li, *Angew. Chem. Int. Ed.* **2022**, *61*, e202116934; *Angew. Chem.* **2022**, *134*, e202116934.

[29] S. Hou, L. Xu, X. Ding, R. M. Kluge, T. K. Sarpey, R. W. Haid, B. Garlyyev, S. Mukherjee, J. Warnan, M. Koch, S. Zhang, W. Li, A. S. Bandarenka, R. A. Fischer, *Angew. Chem. Int. Ed.* **2022**, *61*, e202201610; *Angew. Chem.* **2022**, *134*, e202201610.

[30] C. Kuai, Z. Xu, C. Xi, A. Hu, Z. Yang, Y. Zhang, C.-J. Sun, L. Li, D. Sokaras, C. Dong, S.-Z. Qiao, X.-W. Du, F. Lin, *Nat. Catal.* **2020**, *3*, 743–753.

[31] R. Farhat, J. Dhainy, L. I. Halaoui, *ACS Catal.* **2020**, *10*, 20–35.

[32] C. Feng, F. Wang, Z. Liu, M. Nakabayashi, Y. Xiao, Q. Zeng, J. Fu, Q. Wu, C. Cui, Y. Han, N. Shibata, K. Domen, I. D. Sharp, Y. Li, *Nat. Commun.* **2021**, *12*, 5980.

[33] F. Beck, R. Kaus, M. Oberst, *Electrochim. Acta* **1985**, *30*, 173–183.

[34] S. Klaus, L. Trotochaud, M.-J. Cheng, M. Head-Gordon, A. T. Bell, *ChemElectroChem* **2016**, *3*, 66–73.

[35] I. Spanos, A. A. Auer, S. Neugebauer, X. Deng, H. Tüysüz, R. Schlögl, *ACS Catal.* **2017**, *7*, 3768–3778.

[36] I. Spanos, M. F. Tesch, M. Yu, H. Tüysüz, J. Zhang, X. Feng, K. Müllen, R. Schlögl, A. K. Mechler, *ACS Catal.* **2019**, *9*, 8165–8170.

[37] F. T. Haase, A. Rabe, F.-P. Schmidt, A. Herzog, H. S. Jeon, W. Frandsen, P. V. Narangoda, I. Spanos, K. Friedel Ortega, J. Timoshenko, T. Lunkenbein, M. Behrens, A. Bergmann, R. Schlögl, B. Roldan Cuenya, *J. Am. Chem. Soc.* **2022**, *144*, 12007–12019.

[38] K. Klyukin, K. M. Rosso, V. Alexandrov, *J. Phys. Chem. C* **2018**, *122*, 16086–16091.

[39] M. B. Stevens, C. D. M. Trang, L. J. Enman, J. Deng, S. W. Boettcher, *J. Am. Chem. Soc.* **2017**, *139*, 11361–11364.

[40] L. Bai, S. Lee, X. Hu, *Angew. Chem. Int. Ed.* **2021**, *60*, 3095–3103; *Angew. Chem.* **2021**, *133*, 3132–3140.

[41] K. Fominykh, P. Chernev, I. Zaharieva, J. Sicklinger, G. Stefanic, M. Döblinger, A. Müller, A. Pokharel, S. Böcklein, C. Scheu, T. Bein, D. Fattakhova-Rohlfing, *ACS Nano* **2015**, *9*, 5180–5188.

[42] F. Li, Y. C. Li, Z. Wang, J. Li, D.-H. Nam, Y. Lum, M. Luo, X. Wang, A. Ozden, S.-F. Hung, B. Chen, Y. Wang, J. Wicks, Y. Xu, Y. Li, C. M. Gabardo, C.-T. Dinh, Y. Wang, T.-T. Zhuang, D. Sinton, E. H. Sargent, *Nat. Catal.* **2020**, *3*, 75–82.

[43] Q. Daniel, R. B. Ambre, B. Zhang, B. Philippe, H. Chen, F. Li, K. Fan, S. Ahmadi, H. Rensmo, L. Sun, *ACS Catal.* **2017**, *7*, 1143–1149.

[44] J. Lee, N. Tallarida, X. Chen, P. Liu, L. Jensen, V. A. Apkarian, *ACS Nano* **2017**, *11*, 11466–11474.

[45] A. C. T. van Duin, S. Dasgupta, F. Lorant, W. A. Goddard, *J. Phys. Chem. A* **2001**, *105*, 9396–9409.

[46] K. Chenoweth, A. C. T. van Duin, W. A. Goddard, *J. Phys. Chem. A* **2008**, *112*, 1040–1053.

[47] R. V. Mom, J. Cheng, M. T. M. Koper, M. Sprik, *J. Phys. Chem. C* **2014**, *118*, 4095–4102.

[48] P. P. Lopes, D. Y. Chung, X. Rui, H. Zheng, H. He, P. Farinazzo Bergamo Dias Martins, D. Strmcnik, V. R. Stamenkovic, P. Zapol, J. F. Mitchell, R. F. Klie, N. M. Markovic, *J. Am. Chem. Soc.* **2021**, *143*, 2741–2750.

[49] J. Wang, S.-J. Kim, J. Liu, Y. Gao, S. Choi, J. Han, H. Shin, S. Jo, J. Kim, F. Ciucci, H. Kim, Q. Li, W. Yang, X. Long, S. Yang, S.-P. Cho, K. H. Chae, M. G. Kim, H. Kim, J. Lim, *Nat. Catal.* **2021**, *4*, 212–222.

[50] J. Knöppel, M. Möckl, D. Escalera-López, K. Stojanovski, M. Bierling, T. Böhm, S. Thiele, M. Rzepka, S. Cherevko, *Nat. Commun.* **2021**, *12*, 2231.

[51] S. Geiger, O. Kasian, M. Ledendecker, E. Pizzutilo, A. M. Mingers, W. T. Fu, O. Diaz-Morales, Z. Li, T. Oellers, L. Fruchter, A. Ludwig, K. J. J. Mayrhofer, M. T. M. Koper, S. Cherevko, *Nat. Catal.* **2018**, *1*, 508–515.

[52] K. J. J. Mayrhofer, G. K. H. Wiberg, M. Arenz, *J. Electrochem. Soc.* **2008**, *155*, P1.

[53] G. Dong, M. Fang, H. Wang, S. Yip, H.-Y. Cheung, F. Wang, C.-Y. Wong, S. T. Chu, J. C. Ho, *J. Mater. Chem. A* **2015**, *3*, 13080–13086.

[54] R. Chen, C. Yang, W. Cai, H.-Y. Wang, J. Miao, L. Zhang, S. Chen, B. Liu, *ACS Energy Lett.* **2017**, *2*, 1070–1075.

[55] S. G. Ji, H. Kim, H. Choi, S. Lee, C. H. Choi, *ACS Catal.* **2020**, *10*, 3381–3389.

[56] S. Niu, S. Li, Y. Du, X. Han, P. Xu, *ACS Energy Lett.* **2020**, *5*, 1083–1087.

[57] T. Shinagawa, A. T. Garcia-Esparza, K. Takanabe, *Sci. Rep.* **2015**, *5*, 13801.

[58] S. Koch, P. A. Heizmann, S. K. Kilian, B. Britton, S. Holdcroft, M. Breitwieser, S. Vierrath, *J. Mater. Chem. A* **2021**, *9*, 15744–15754.

[59] Y. S. Park, M. J. Jang, J. Jeong, S. M. Park, X. Wang, M. H. Seo, S. M. Choi, J. Yang, *ACS Sustainable Chem. Eng.* **2020**, *8*, 2344–2349.

[60] Y. S. Park, J. Yang, J. Lee, M. J. Jang, J. Jeong, W.-S. Choi, Y. Kim, Y. Yin, M. H. Seo, Z. Chen, S. M. Choi, *Appl. Catal. B* **2020**, *278*, 119276.

[61] J. Lee, H. Jung, Y. S. Park, S. Woo, J. Yang, M. J. Jang, J. Jeong, N. Kwon, B. Lim, J. W. Han, S. M. Choi, *Small* **2021**, *17*, 2100639.

[62] S. S. Jeon, J. Lim, P. W. Kang, J. W. Lee, G. Kang, H. Lee, *ACS Appl. Mater. Interfaces* **2021**, *13*, 37179–37186.

[63] P. Acharya, R. H. Manso, A. S. Hoffman, S. I. P. Bakovic, L. Kékedy-Nagy, S. R. Bare, J. Chen, L. F. Greenlee, *ACS Catal.* **2022**, *12*, 1992–2008.

[64] S. Lee, K. Banjac, M. Lingenfelder, X. Hu, *Angew. Chem. Int. Ed.* **2019**, *58*, 10295–10299; *Angew. Chem.* **2019**, *131*, 10401–10405.

[65] Z. He, J. Zhang, Z. Gong, H. Lei, D. Zhou, N. Zhang, W. Mai, S. Zhao, Y. Chen, *Nat. Commun.* **2022**, *13*, 2191.